Chemical Engineering Science 200 (2019) 12–26

Contents lists available at ScienceDirect

Chemical Engineering Science

journal homepage: www.elsevier.com/locate/ces

Numerical simulation of mono-disperse droplet spray dryer: Coupling distinctively different sized chambers

Jie Xiao [a,*], Shujun Yang [a], Oluwafemi Ayodele George [a], Aditya Putranto [b], Winston Duo Wu [a], Xiao Dong Chen [a,*]

[a] China-Australia Joint Research Center in Future Dairy Manufacturing, School of Chemical and Environmental Engineering, College of Chemistry, Chemical Engineering and Materials Science, Soochow University, Suzhou, Jiangsu Province 215123, People's Republic of China
[b] School of Chemistry and Chemical Engineering, Queens University Belfast, Belfast BT71NN, UK

HIGHLIGHTS

- Modeling the mono-disperse droplet spray dryer (MDSD) as a holistic unit.
- Coupling the small dispersion chamber and the big drying chamber of the MDSD.
- Numerical simulation of droplets flying through distinctively different sized chambers.
- Smooth transition of droplets from one chamber to the other by a coupling method.

GRAPHICAL ABSTRACT

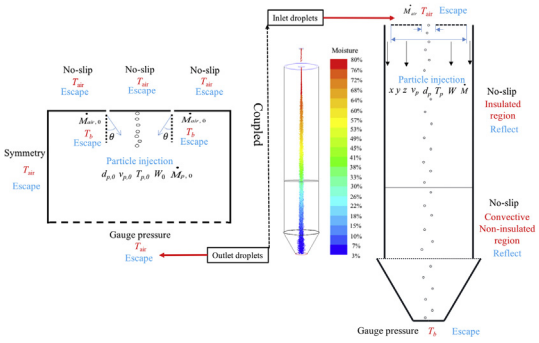

ARTICLE INFO

Article history:
Received 9 April 2018
Received in revised form 2 October 2018
Accepted 12 January 2019
Available online 8 February 2019

Keywords:
Mono-disperse droplet spray dryer
CFD simulation
Discrete phase model
Reaction engineering approach (REA)
Skim milk powder

ABSTRACT

The discrete phase model (DPM) has been widely used in CFD simulations to track discrete particles or droplets in a continuum fluid filed. This powerful technique, however, may face tremendous difficulty in tracking droplets flying through chambers with significantly different sizes. In such cases, it becomes very challenging to develop effective mesh for the big and small chambers together with the transition zone that can ensure solution convergence within reasonable computational time. In this work, a systematic method is introduced to tackle this problem. This method allows simulation of different sized chambers separately to avoid the meshing difficulty. A unique coupling approach offers smooth transition of droplets from one chamber to the other with rigorous conservation of their mass, energy and momentum. The effectiveness of the method is demonstrated through the simulation of skim milk droplet drying in a mono-disperse droplet spray dryer (MDSD), where droplets must pass through a small dispersion chamber before entering the main big drying chamber. For the first time, droplet drying process from exiting nozzle to the arrival at the dryer outlet can be simulated. The new model can be used in the future to optimize the spray drying process.

1. Introduction

Spray drying is a conventional technology for converting large quantities of liquid into powder products in short time with many industrial applications such as foods, pharmaceuticals, and chemical industries, etc. (Liu et al., 2011; Rogers et al., 2012; Vicente

* Corresponding authors.
E-mail addresses: jie.xiao@suda.edu.cn (J. Xiao), xdchen@mail.suda.edu.cn (X.D. Chen).

https://doi.org/10.1016/j.ces.2019.01.030
0009-2509/

Nomenclature

A_p	droplet/particle surface area (m^2)
a_w	water activity
C	GAB isotherm model parameter
C_p	specific heat under constant pressure ($J\,kg^{-1}\,K^{-1}$)
d	droplet/ particle diameter (m)
ΔE_v	apparent activation energy ($J\,mol^{-1}$)
$\Delta E_{v,b}$	equilibrium activation energy ($J\,mol^{-1}$)
ΔH_L	latent heat of water vaporization ($J\,kg^{-1}$)
h	heat transfer coefficient ($W\,m^{-2}\,K^{-1}$), enthalpy
h_m	mass transfer coefficient ($m\,s^{-1}$)
$\vec{J}_j$	diffusion flux of species j
K	GAB isotherm model parameter
k_{eff}	effective conductivity
m	mass (kg)
$\dot{M}$	mass flow rate (kg/s)
n	droplet number in computational mesh cell
N	collected droplet number
R_H	relative humidity
R	universal gas constant
T	temperature (K)
w_0	monolayer moisture content ($kg\,kg^{-1}$)
W	moisture content (wb) ($kg\,kg^{-1}$)
X	moisture content (db) ($kg\,kg^{-1}$)

Greek symbols

α	coefficient for linear shrinkage models
ρ	density ($kg\,m^{-3}$)

Superscripts

w	water
s	solid

Subscripts

b	bulk
e	equilibrium
p	particle
s	surface/solid
v	vapor
w	water
0	initial

et al., 2013; You et al., 2014). From merely producing huge capacity of powders it is traditionally known for, spray drying has advanced to the present stage of controlling the functionalities of the particles (Ré, 2006; Baldwin and Truong, 2007; Sagadin and Hriberšek, 2017). In response to the new desire, immense efforts have been invested into the design of the modern-day spray dryers and nozzle jets. This of course, is aimed towards facilitating easy dispersion of droplets into a spray with consistent morphology and achieving sufficiently dried outlet powders to meet specified standards (Xiao et al., 2018). Uniform particle size is also, for instance, desirable in maximizing the potency of drug delivery system (Ré, 2006). As much of the progress that has been made in terms of increasing production output, improving powder quality and reducing costs, full understanding of the process and a robust control implementation strategy, yet remain the challenges facing both the designers and users (Huang et al., 2003; Woo et al, 2008; Xiao and Chen, 2014; Yang et al, 2015; George et al., 2015; Xiao et al., 2018).

Depending on the material feeds to be dried, two main categories of spray dryers are commonly being employed, i.e. counter-current and co-current types. Readers are referred to (Baltas and Gauvin, 1969; Shakiba et al., 2016) for more details about the dryers operation. The latter types have largely been applied for heat sensitive materials, e.g. milk, and is considered relevant in this discussion. Usually, the liquid feeds are passed in the same direction with the streams of hot gas; where simultaneous exchange of mass and heat results in the removal of excess moisture (Vicente et al., 2013). The fate of each outlet particle is determined by its trajectory experience within the dryer. Under a relatively high intensity of air flow in a typical spray dyer, droplets trajectories might not be uniformly controlled (Jin and Chen, 2009b). This constitutes a huge problem in particle quality control. These challenges led to the development of a simple and robust set-up that provides precise control of the spray drying operation, known as mono-disperse droplet spray dryer (MDSD) (Woo et al., 2012;You et al., 2014; Yang et al., 2015; Foerster et al., 2016).

A schematic arrangement of a mono-disperse droplet spray dryer, comprising of the nozzle, the dispersion chamber and the main drying column is displayed in Fig. 1. The unique nozzle design allows generation of mono-dispersed droplets. A uniformly controlled particle drying history can be ensured (Woo et al., 2012). Furthermore, each atomized droplet in a typical MDSD passes through the dispersion chamber, then to the main chamber where rigorous drying takes place. This dryer arrangement is often a prerequisite to produce completely dried powders for MDSD systems. To be more specific, the outcomes of the reports from past experiments show that (i) absence of droplet pre-dispersion can result in an inefficient drying (i.e. wet particles), and (ii) operating settings of the dispersion chamber significantly affect the distribution of droplets. These observations led to further studies on the subject matter to address the effects of droplet pre-dispersion in the dispersion chamber on the final particle condition. However, due to experimental limitations, the dispersion dynamics cannot be readily observed. The key factors that might influence droplet dispersion remain vague and un-probed. Exploring this phenomenon by resorting to numerical simulation becomes necessary.

To a very great extent, simulation tools such as COMSOL Multiphysics, FLOW3D, ANSYS fluent or even MATLAB and EXCEL, have been employed by many authors to explore dryer-wide spray drying scenarios (Chen and Lin, 2005; Mezhericher et al., 2007, 2008; Patel and Chen, 2008; Fletcher and Langrish, 2009; Mezhericher et al., 2014; George et al., 2015; Kavoshi et al., 2015; Pawar et al., 2015). Earliest reports on modelling for MDSD can be credited to Woo et al. (2011). In general, agglomeration, wall deposition, powder quality degradation, etc. are the commonly examined phenomena, and have been investigated to a far-reaching extent. However, the focus of these studies have been limited to the main drying chamber (Woo et al., 2012; Yang et al., 2015). Not until the year 2011 was there a first reported case of modelling work on the dispersion chamber that links the nozzle jet to the main dryer for MDSD system (Woo et al., 2011). They examined the unusual characteristics and possible improvements for MDSD by using four droplet injection points to approximate the dispersed state of droplets at the outlet of the dispersion chamber, which is also the inlet of the main drying chamber. Based on this work, Yang et al. (2015) assumed five droplet injection points in order to obtain a more "realistic" dispersed state. Nevertheless, the 2D model of Woo et al. (2011) and the 3D model of Yang et al. (2015), are unrealistic, since the droplet pre-dispersion in the dispersion chamber was not modeled and the dispersed state was

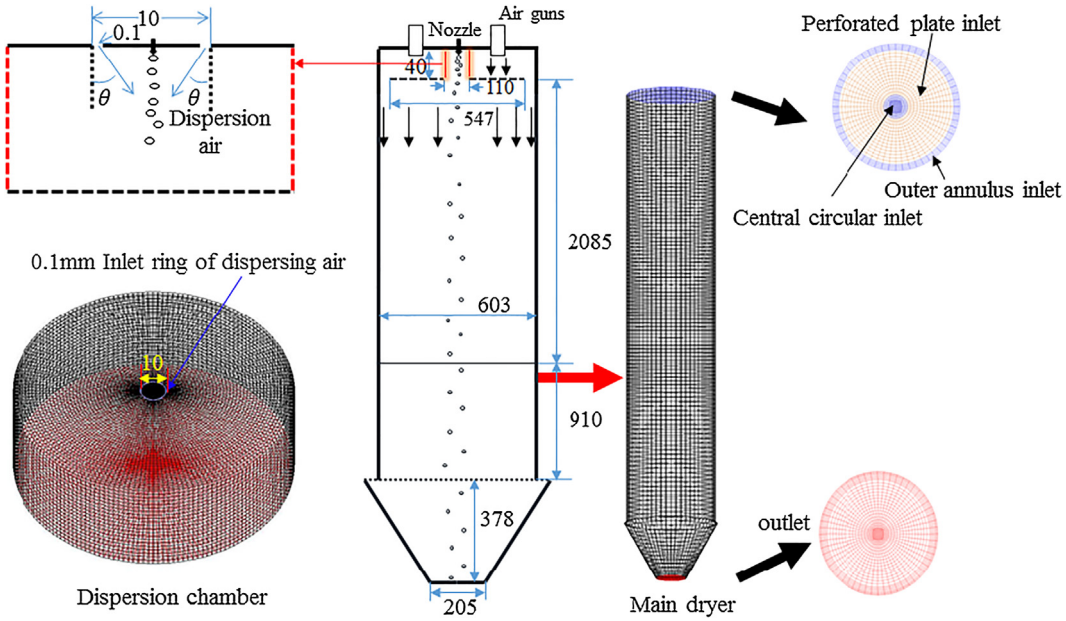

Fig. 1. Schematic diagram of the mono-disperse droplet spray dryer (dimension: mm).

assumed by the authors. Most recently, Xiao et al. (2018) conducted a comprehensive numerical analysis for droplet predispersion in the dispersion chamber of an MDSD. The study allowed the dispersion of droplets in the dispersion chamber to be visualized. It also offered systematic and quantitative data analyses for improved design of the dispersion chamber. Nonetheless, the significant size difference between the dispersion and the main drying columns made numerical coupling of the whole system as a single unit very challenging.

It has become very apparent that coupling of the dispersion chamber and main dryer is very paramount for tracking particles' complete drying process. Numerical simulation of discrete phase particles flying through distinctively different sized chambers appears to be largely unexplored. The current work presents an effective method for tackling this challenging problem. By resorting to this method, the entire MDSD system for drying of skim milk droplets can be simulated using ANSYS Fluent with the incorporation of a reliable drying model, i.e. reaction engineering approach (REA). The introduced method allows simulation of different sized chambers separately to avoid the meshing difficulty. A strategic coupling approach offers smooth transition of droplets from one chamber to the other with rigorous conservation of their mass, energy and momentum. To the best of our knowledge, such study has never been investigated.

2. Modelling and analysis method

2.1. Problem statement and system description

Schematic representation of mono-disperse droplet spray dryer used in the simulation is shown in Fig. 1. The experience of an individual droplet in the main chamber or the fate of each outlet product (whether dry or wet) is highly influenced by the dynamics of the dispersed droplets in the dispersion chamber. Recently, detailed numerical simulations were conducted to quantify droplets' dynamics in the dispersion chamber (Xiao et al., 2018). The study was restricted to the dispersion segment due to the great challenge in coupling with the main dryer. The volume ratio of the dispersion chamber to the main drying zone is in the order of 1:2000. Droplet dispersion is achieved by the introduction of dispersion air from a ring shaped slit located at the top surface of the small dispersion chamber. As shown in Fig. 1, the diameter of the ring inlet is 10 mm and the width of the slit is only 0.1 mm (i.e. 1/1100 of the diameter of the dispersion chamber, or 1/6030 of the diameter of the drying chamber). Furthermore, the inlet angle of dispersion air should be adjustable. In order to properly simulate droplet dispersion under the influence of the dispersion air, a very fine mesh has to be used for the dispersion chamber. The total number of cells for this small chamber is 229,152. The minimum cell volume is 1.068053×10^{-11} m^3, while the maximum cell volume is 4.891153×10^{-9} m^3. On the other hand, droplet flying in the drying chamber is influenced by the hot air whose inlet flow is made uniformly distributed with a downward direction through the specially designed perforated plate (Fig. 1). Thus, a coarser grid with 162,904 cells can be used for the drying chamber. The sizes of the maximum and minimum cells are respectively 1.450679×10^{-5} m^3 and 4.902243×10^{-8} m^3. The maximum mesh cell volume of the main dryer is more than 10^3 times larger when compared with the maximum mesh cell volume of the dispersion chamber. Therefore, it is not effective or even not practical to simulate the dispersion chamber and the drying chamber as a single unit.

To circumvent these difficulties, a coupling scheme has been developed in which the statistics of the droplets exiting the dispersion chamber are initially recorded. The recorded droplets are then mapped to the corresponding inlet locations of the main dryer, and serve as the input conditions for the main drying chamber. The discrete phase model (DPM) has been combined with the drying rate model to effectively describe the physical behavior of drying of skim milk droplets. The model framework is given in Fig. 2. Two chambers simulated separately are coupled using a special scheme which will be introduced later with great details.

2.2. Governing equations

In both chambers, a discrete phase model (DPM) has been utilized to track droplets. The bulk fluid is captured by 3D Navier-Stokes conservation equations integrated with a drying rate model to describe the air/ particle flow behaviors during mass, energy and momentum exchange. In this study, reaction engineering approach

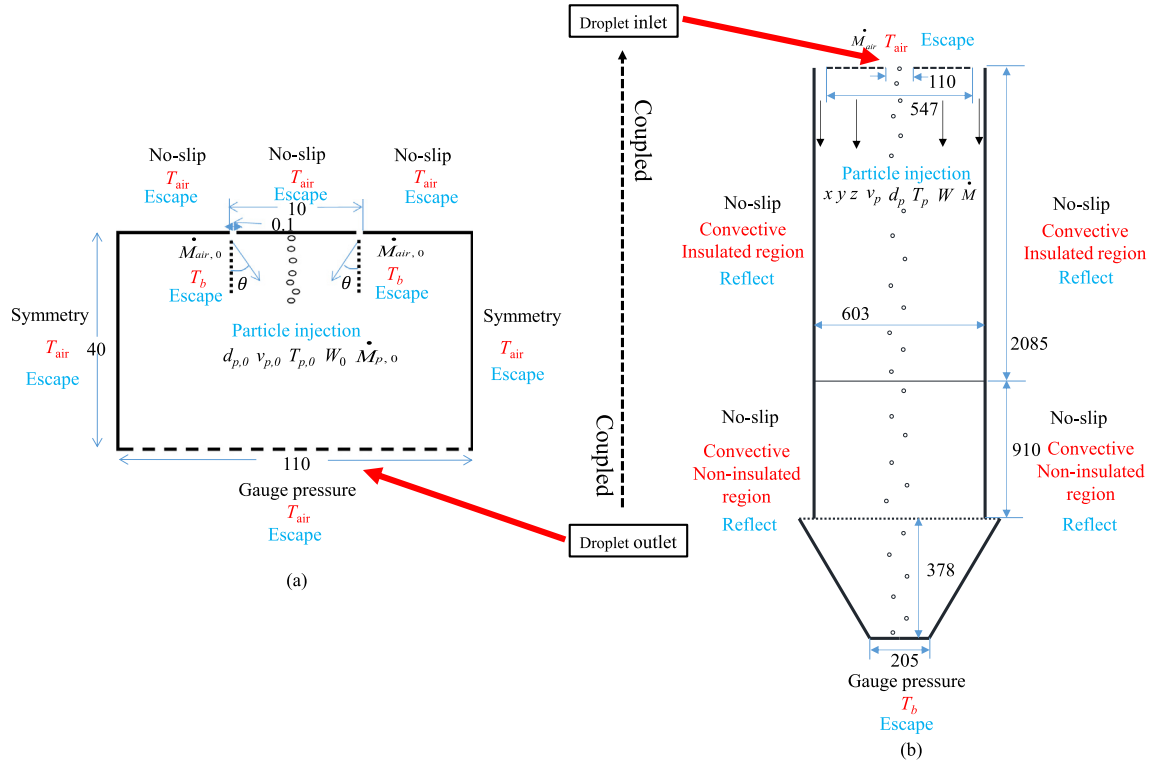

Fig. 2. Cross sectional view of two coupled simulation domains with boundary conditions: (a) the dispersion chamber and (b) the main drying chamber (dimension: mm).

(REA) has been used to describe the physical attributes of droplets during drying (Chen and Lin, 2005; Chen, 2008; Patel et al., 2009; Putranto and Chen, 2016; Schmitz-Schug et al., 2016).

Two-way coupling of the continuous phase and dispersed droplets was implemented in this work. In other words, the interphase exchange of heat, mass, and momentum between the air and the droplet has been fully taken into account. This coupling was achieved through alternately solving the continuous and discrete phase equations until obtaining converged solutions in both phases. The RNG k-ε turbulent model has been utilized to model the slightly turbulent flow in the chamber. The discrete droplet phase has been combined with the gas phase using a particle drag model (Haider and Levenspiel, 1989; Patel et al., 2010; Zastawny et al., 2012). The drag and buoyant forces exerted by air, as well as the gravitational force drive droplet acceleration,

$$\frac{d\vec{v}_p}{dt} = \frac{C_D 18\mu_b Re\left(\vec{v} - \vec{v}_p\right)}{24\rho_p d_p^2} + \frac{g}{\rho_p}\left(\rho_p - \rho_b\right) \tag{1}$$

The first expression on the right side of Eq. (1) corresponds to the drag force per unit mass due to air-droplet relative motion. The second expression represents the difference between the buoyancy and gravitational forces per unit mass. The velocity vectors (m/s) of droplet and gas are respectively denoted as $\vec{v}_p$ and $\vec{v}$. An empirical correlation (Patel et al., 2010) was used to calculate the drag coefficient, C_d by relating Reynolds number (Re) to C_d. The virtual mass force, lift force and Basset force were not taken into account. The virtual mass effect is significant when the secondary phase density is much smaller than the primary phase density. However, the primary phase in this work has a much lower density. The Saffman's lift force is recommended to be used only for submicron particles, which is not applicable to this study. The size of a particle in this work is more than ten times larger than 1 μm. The influence of the Basset force can be neglected when the fluid-to-particle density ratio is less than 0.002 (Vojir and Michaelides, 1994; Song et al., 2016). The ratio in this study is less than 0.001 (i.e., the air-to-water density ratio). This ratio decreases as drying proceeds due to the increase of droplet density (from wet to dry). Thus the Basset force can be safely neglected as well. The transfer of momentum from the droplet to the air was then implemented as a momentum sink in the continuous phase momentum balance equation.

The shape of a falling droplet has been assumed spherical, thus drying causes uniform shrinkage of the droplet diameter, d_p. A linear shrinkage model proposed by Lin and Chen (2004) was deemed suitable to estimate droplet shrinkage behavior. The droplet diameter, d_p, is linearly related to its moisture content, X,

$$\frac{d_p}{d_{p,0}} = \alpha + (1-\alpha)\frac{X}{X_0} \tag{2}$$

where $d_{p,0}$ and X_0 are the droplet's initial diameter (m) and initial moisture content (kg/(kg, db)) respectively; α is 0.59 for 20 wt% skim milk droplets.

The driving force for drying is the difference between the droplet and gas vapor concentrations according to REA (Patel and Chen, 2008). The conservation of heat between the droplet and gas involving moisture removal can be calculated by using the following equations (Yang et al., 2015):

$$\begin{cases} \frac{dT_p}{dt} = \frac{hA_p\left(T_b - T_p\right) + \Delta H_L \frac{dm_p}{dt}}{m_w C_{p,w} + m_s C_{p,s}} \\ \frac{\partial}{\partial t}(\rho E) + \nabla \cdot \left[\vec{v}(\rho E + P)\right] = \nabla \cdot \left[k_{eff}\nabla T_b - \sum_j h_j \vec{J}_j + \left(\vec{\tau}_{eff} \cdot \vec{v}\right)\right] - n\frac{dm_p}{dt}h_{H2O(g)} \end{cases} \tag{3}$$

where T_p and T_b are the droplet and air temperatures (K) respectively; h is the heat transfer coefficient (W/(m^2·K)) (Ranz and Marshall, 1952a, 1952b); n is the number of droplets in a computational mesh cell; h_{H2O} is defined as the vapor specific enthalpy (J/kg); m_p corresponds to the mass of one particle. The last term on the right hand side of Eq. (3) (i.e. second expression) corresponds to energy sink due to drying.

Evaporation causes the transfer of moisture from the droplet to the gas phase. This is denoted mathematically as (Yang et al., 2015),

$$\begin{cases} -m_s \frac{dX}{dt} = h_m A_p \left(\rho_{v,s} - \rho_{v,b}\right) \\ \frac{dm_{air}}{dt} = n h_m A_p \left(\rho_{v,s} - \rho_{v,b}\right) \end{cases} \tag{4}$$

The rates of moisture removal and moisture gain from the droplet and bulk gas are given respectively in Eq. (4). The mass transfer coefficient, h_m (m/s) can be obtained from the modified form of the Ranz and Marshall correlations (Ranz and Marshall, 1952a, 1952b). The bulk gas vapor concentration (kg/m^3) is $\rho_{v,b}$, and $\rho_{v,s}$ denotes the vapor concentration at the droplet-gas phase boundary (kg/m^3) given as,

$$\rho_{v,s} = \exp\left(-\frac{\Delta E_v}{RT_p}\right)\rho_{v,sat}(T_p) \tag{5}$$

The apparent activation energy, ΔE_v, can be quantified from the equilibrium activation energy, $\Delta E_{v,e}$ and the droplet moisture content, X as;

$$\frac{\Delta E_v}{\Delta E_{v,e}} = a \cdot \exp\left[-b(X - X_e)^c\right] \tag{6}$$

where a = 0.998, b = 1.405 and c = 0.930 are the material dependent constants for 20 wt% skim milk (Rogers et al., 2012). The equilibrium moisture content of particle in the bulk gas phase, X_e can be obtained using Guggenheim-Anderson-de Boer (GAB) desorption isotherm model given as (Lin et al., 2005),

$$X_e = w_0 \frac{CKa_w}{(1 - Ka_w)(1 - Ka_w + CKa_w)} \tag{7}$$

where a_w is the water activity in the bulk gas; W_0 is the monolayer moisture content; parameters C and K are functions of gas temperature,

$$\begin{cases} C = C_0 \cdot exp\left(\frac{\Delta H_1}{RT_b}\right) \\ K = K_0 \cdot exp\left(\frac{\Delta H_2}{RT_b}\right) \end{cases} \tag{8}$$

where for skim milk, W_0 = 0.06156; C_0 = 0.001645; K_0 = 5.71; ΔH_1 = 24831 J/mol; ΔH_2 = −5118 J/mol.

2.3. Boundary conditions

The boundary conditions for mass, momentum and heat conservation equations are shown in the cross-sectional view of the cylindrical dispersion and the main drying chambers (Fig. 2). A circular slit with a thickness of 0.1 mm opens the passage for the dispersed air flow into the dispersion chamber (see Fig. 2(a)). The lower end of the chamber is the outlet with a gauge pressure. A constant hot air temperature is used for the solid walls to satisfy the requirement of heating up the column to a steady state before introduction of droplets in experimental MDSD. Atomized droplets with certain initial size, temperature, mass flow rate and moisture content are injected vertically downwards into the dispersion chamber. The bottom of the column leads droplet passage directly to the main dryer. The 'escape' boundary condition can be implemented in ANSYS Fluent through a boundary selection, and is used to discontinue the activity of such droplets hitting the boundaries. As soon as droplets touch the surface, their trajectory calculations are terminated. The specific values of boundary conditions used in this study for the dispersion chamber are listed in Table 1.

The location, size, temperature and moisture content of droplets exiting the bottom surface of the dispersion chamber are recorded and mapped to a certain number of droplet injections for the main dryer (Fig. 2). The coupling scheme will be introduced in the next section. The main tower is divided into two parts with different levels of thermal insulation, i.e. convective insulated and non-insulated regions (Fig. 2(b)). Particles are collected at the bottom outlet with a gauge pressure. Unlike in the dispersion chamber where an 'escape' condition is used, the 'reflect' boundary condition in ANSYS *Fluent* has been used for particles hitting at all walls in this dryer segment. The velocity of particles is obtained by (Jin and Chen, 2009a, 2009b).

Table 1
Initial and boundary conditions for the dispersion chamber.

Fluid parameters:	
Inlet flow rate of dispersion air (L min^{-1})	0.5
Initial hot air temperature (°C)	90, 111, 135, 157, 183
Initial dispersion air temperature (°C)	25
Inlet angel (°)	43
Droplet parameters:	
Initial particle size (μm)	191, 195, 200, 186, 181
Mass flow rate (kg s^{-1})	3×10^{-5}
Initial velocity (m s^{-1})	1
Initial droplet temperature (°C)	25
Initial moisture content (%)	80

$$\begin{cases} \vec{V}_{n,out} = -\vec{V}_{n,in} \\ \vec{V}_{t,out} = \vec{V}_{t,in} \end{cases} \tag{9}$$

where $\vec{V}_{n,out}$ and $\vec{V}_{t,out}$ are normal and tangential velocity components to the wall after reflection respectively. All the boundary condition values can be found in Tables 1 and 2.

2.4. Coupling the dispersion chamber and the main drying chamber

This section introduces an effective scheme to couple DPM models for chambers with distinctively different sizes. Simulating the complete drying process from droplet generation to particle collection in a mono-disperse droplet spray dryer becomes possible.

Table 2
Initial and boundary conditions for the drying chamber.

Central inlet of hot air:	
Mass flow rate (kg s^{-1})	2.478e−3
Direction	Normal
Water vapor mass fraction (kg H_2O/kg air)	0.01
Temperature (°C)	90, 111, 135, 157, 183
Annulus inlet of hot air:	
Mass flow rate (kg s^{-1})	7.816e−4
Direction	Normal
Temperature (°C)	90, 111, 135, 157, 183
Water vapor mass fraction (kg H_2O/kg air)	0.01
Outer annulus inlet of hot air:	
Mass flow rate (kg s^{-1})	1.152e−5
Direction	Normal
Temperature (°C)	90, 111, 135, 157, 183
Water vapor mass fraction (kg H_2O/kg air)	0.01
Outlet:	
Gauge pressure (pa)	0
Backflow temperature (°C)	25
Wall:	
Convective heat transfer coefficient of the insulated region (W m^{-2} K^{-1})	2, 2, 2, 2, 2
Convective heat transfer coefficient of the non-insulated region (W m^{-2} K^{-1})	5, 8, 8, 8, 8
Room temperature (°C)	25

2.4.1. Data collection for droplets exiting the dispersion chamber

In order to provide droplet inlet conditions for numerical simulation of the main drying chamber, the property data of all droplets exiting the dispersion chamber are collected at the outlet plane. These date include droplet location (x, y, z), velocity $(\vec{v}_p)$, temperature (T_p), diameter (d_p), moisture content (W), and mass (m_p). In addition, the total number of collected droplets (N) at the outlet plane is also counted.

2.4.2. Identification and division of droplet-occupied area

Droplets exiting the outlet plane of the dispersion chamber are plotted in that plane based on their locations (see Fig. 3(a)). In this particular case, droplet diameter (d_p) is represented by the color bar. Fig. 3(a) shows that most droplets occupy an area close to the center of the surface. A circular area with a radius of r_{max} can be readily identified that can cover majority droplets (e.g., 98%) (see the area circled by the black line in Fig. 3(b)).

Following the determination of droplet-occupied area, this area can be further divided into a number of zones. In each zone, droplets' statistics can be used to design a droplet injection, which is expected to generate a stream of droplets demonstrating the same statistics as those droplets collected in the zone. Four different schemes have been designed to divide the area, and used to couple the dispersion chamber with the main dryer (see Fig. 3(c)). An injection can be created in each zone which continuously generates droplets into the main drying chamber. The circular area of radius r_{max} is divided into k layers with each layer containing four sub-division zones represented by "j" (refer to Fig. 4 for illustration on slice division). In the design scheme 1, a total of 12 zones are obtained and the thickness of each k layer is equal (see Fig. 4(a)), i.e.,

$$\frac{r_{max}}{3}(k-1) < r \le \frac{r_{max}}{3}k \quad k = 1, 2, 3 \tag{10}$$

In the design scheme 2, another layer has been added to the innermost circle as shown in Fig. 4(b). Since majority of the droplets are concentrated around the central region (see Fig. 3(b)), scheme 2 has been developed in order to make the number of droplets in each zone more uniform. The distance of each spaced layer from the circle center can be obtained from,

$$\begin{cases} 0 < r \le \frac{1}{6}r_{max} & (k=1) \\ \frac{1}{6}r_{max} < r \le \frac{1}{3}r_{max} & (k=2) \\ \frac{1}{3}r_{max} < r \le \frac{2}{3}r_{max} & (k=3) \\ \frac{2}{3}r_{max} < r \le r_{max} & (k=4) \end{cases} \tag{11}$$

Sixteen injection points are generated on top of the main dryer for scheme 3, with each layer corresponding to 25% of the total number of droplets (see Fig. 4(c)). The design scheme 4 is similar to scheme 3 on the basis of equal number of injection points and spacing of each layer. The injection location is, however, rotated by 45° (see Fig. 4(d)).

Schemes 1 and 2 would offer significantly different numbers of droplets from each injection. Specifically, the number of droplets generated from an injection in the outer layer could be significantly smaller than that from an injection in the inner layer. However, schemes 3 and 4 would offer injections that can generate droplets of the same flow rate. Thus the characteristics of droplets in the outer layer could be better captured by such kind of uniform mass flow rate based division scenario. Compared with "X" shaped distribution of injections in schemes 1–3 (Fig. 4), the "star" (*) shaped distribution in scheme 4 may better capture the dispersed state of droplets in the dispersion chamber.

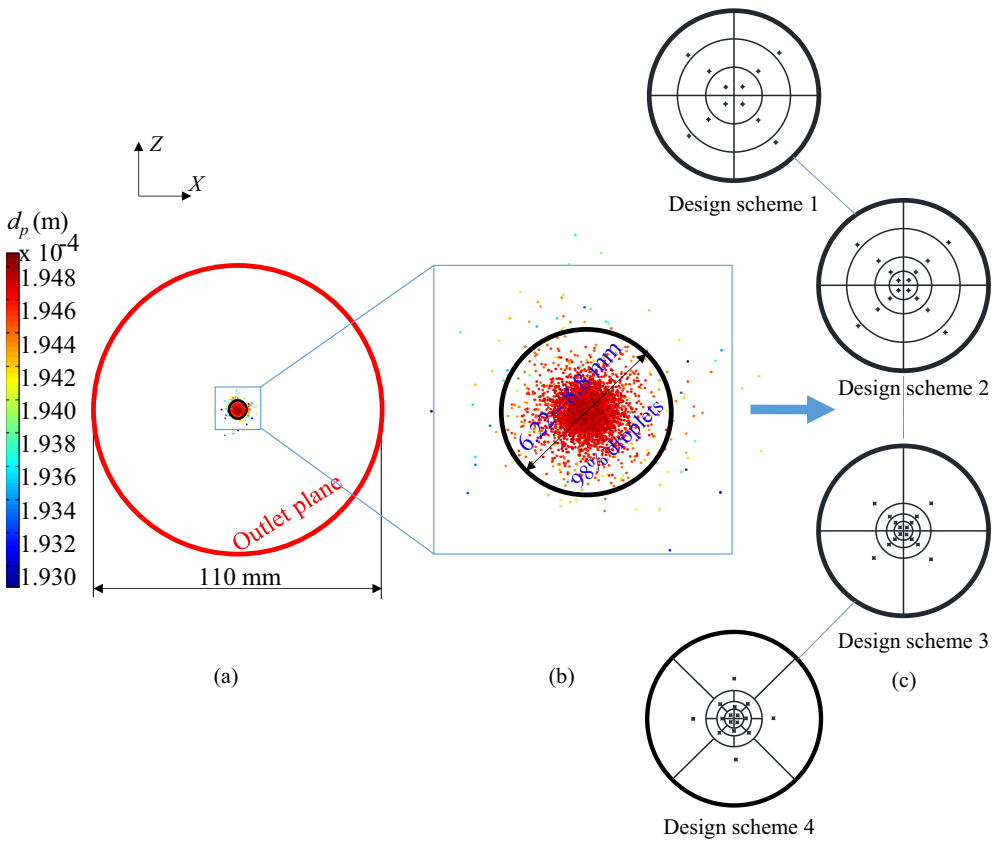

Fig. 3. Identification of the droplet-occupied area together with its division.

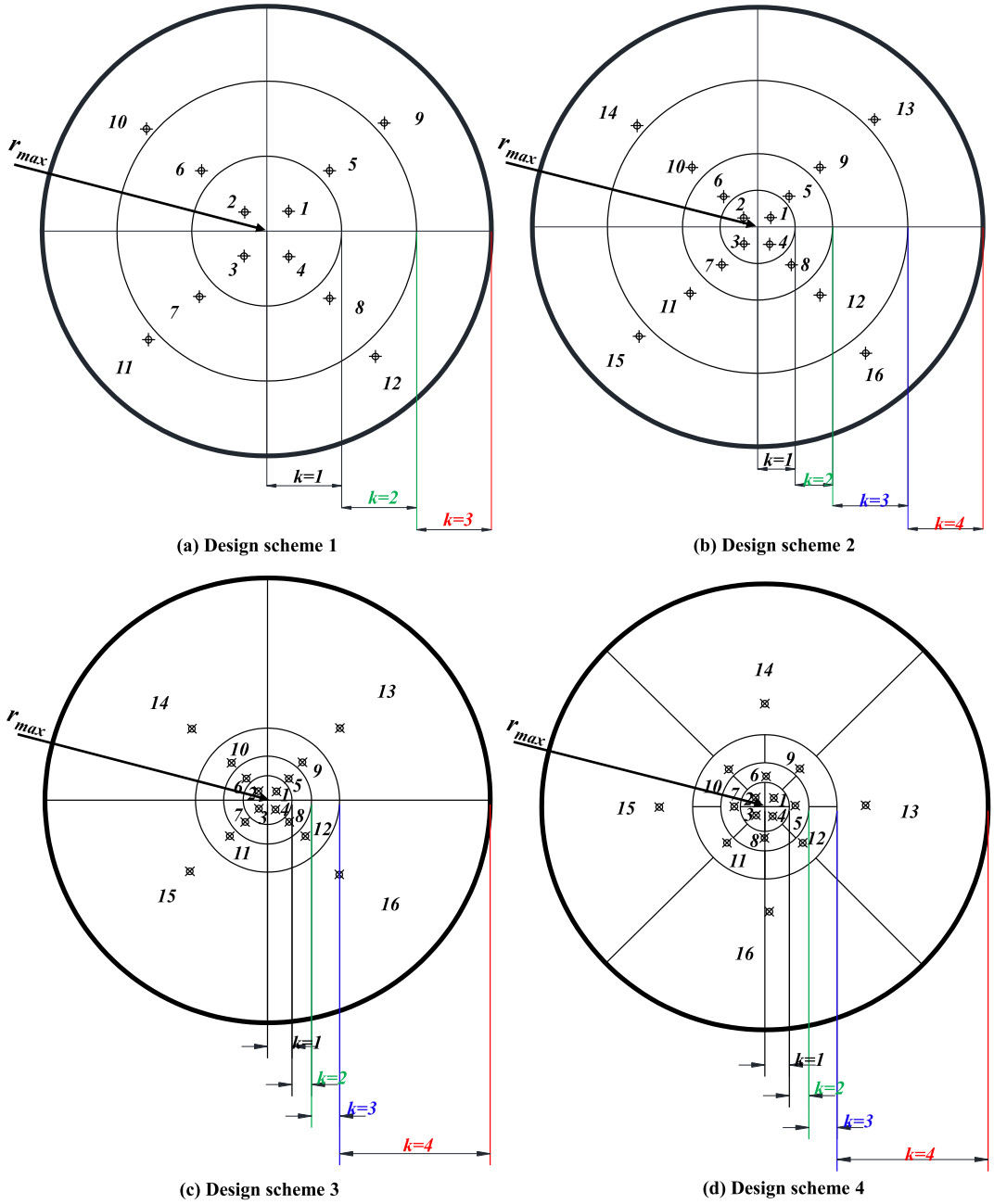

Fig. 4. Illustration of spatial division schemes for the droplet-occupied area.

2.4.3. Creating injections

One injection can be created in each zone to generate a stream of droplets to be injected into the drying chamber. The settings of the injection should be calculated based on the conservations of mass, momentum and energy for droplets passing across the coupling interface. Droplets are not uniformly distributed in each zone, thus the location of the j-th injection is taken as the average location of all N_j droplets collected in the j-th zone, i.e.

$$\begin{cases} \bar{x}_j = \frac{1}{N_j}\sum_{i=1}^{N_j} x_{i,j} \\ \bar{y}_j = 0 \\ \bar{z}_j = \frac{1}{N_j}\sum_{i=1}^{N_j} z_{i,j} \end{cases} \tag{12}$$

Droplets conserve momentum while passing through the coupling interface. The initial velocity of droplets from the j-th injection is then,

$$\begin{cases} \bar{u}_j = \frac{1}{\sum_{i=1}^{N_j} m_{i,j}}\sum_{i=1}^{N_j} m_{i,j}u_{i,j} \\ \bar{v}_j = \frac{1}{\sum_{i=1}^{N_j} m_{i,j}}\sum_{i=1}^{N_j} m_{i,j}v_{i,j} \\ \bar{w}_j = \frac{1}{\sum_{i=1}^{N_j} m_{i,j}}\sum_{i=1}^{N_j} m_{i,j}w_{i,j} \end{cases} \tag{13}$$

Although the residence time of droplets in the dispersion chamber is short, solvent evaporation and rising of the droplet temperature also occur in the dispersion chamber. The temperature, moisture content and diameter of droplets from the j-th injection can be obtained respectively through,

$$\bar{T}_j = \frac{\sum_{i=1}^{N_j}\left(m_{i,j}^{w}Cp_w + m_{i,j}^{s}Cp_s\right)\cdot T_{i,j}}{N_j\left(m_w Cp_w + m_s Cp_s\right)} \tag{14}$$

$$\bar{W}_j = \frac{\sum_{i=1}^{N_j} m_{i,j} - N_j m_s}{\sum_{i=1}^{N_j} m_{i,j}} \tag{15}$$

$$\bar{d}_j = \sqrt[3]{\frac{\sum_{i=1}^{N_j} (d_{i,j})^3}{N_j}} \tag{16}$$

To ensure continuous supply of droplets to the drying chamber, the mass flow rate of each injection needs to be defined. The total mass flow rate of mono-disperse nozzle is known, i.e. $\dot{M}_0$. The mass flow rate of each injection ($\dot{M}_j$) can be determined by,

$$\begin{cases} \dot{M}_j = \frac{\sum_{i=1}^{N_j} m_{i,j}}{\sum_{i=1}^{N} m_i} \dot{M}_0 \left(1 - \frac{M_{vap}}{N m_0}\right) \\ M_{vap} = N m_0 - \sum_{i=1}^{N} m_i \end{cases} \tag{17}$$

where m_0 and N are the droplet's initial mass (kg) and the total number of collected droplets respectively; the total evaporation in the dispersion chamber is M_{vap}.

2.4.4. Procedures for the coupled scheme

Procedures taken to couple the dispersion model and the main drying model shown in Fig. 2 are summarized by the following steps.

Step 1. Develop a 3D dispersion chamber model to solve the mass, momentum and energy conservation equations for $||\vec{v}_p||$, W, d_p and T_p. Continue this step until pre-specified number of droplet samples have been "collected" at the outlet plane (i.e., the bottom surface of the dispersion chamber, see Fig. 3 (a)).

Step 2. Identify the droplet occupied area and divide such area into a number of zones based on an appropriate scheme.

Step 3. Create an injection in each zone and calculate the parameters as inlet droplet initial conditions of the main drying chamber using Eqs. (12)–(17).

Step 4. Develop a 3D model for the main drying chamber and adopt the parameters obtained from *Step* 3. This step should

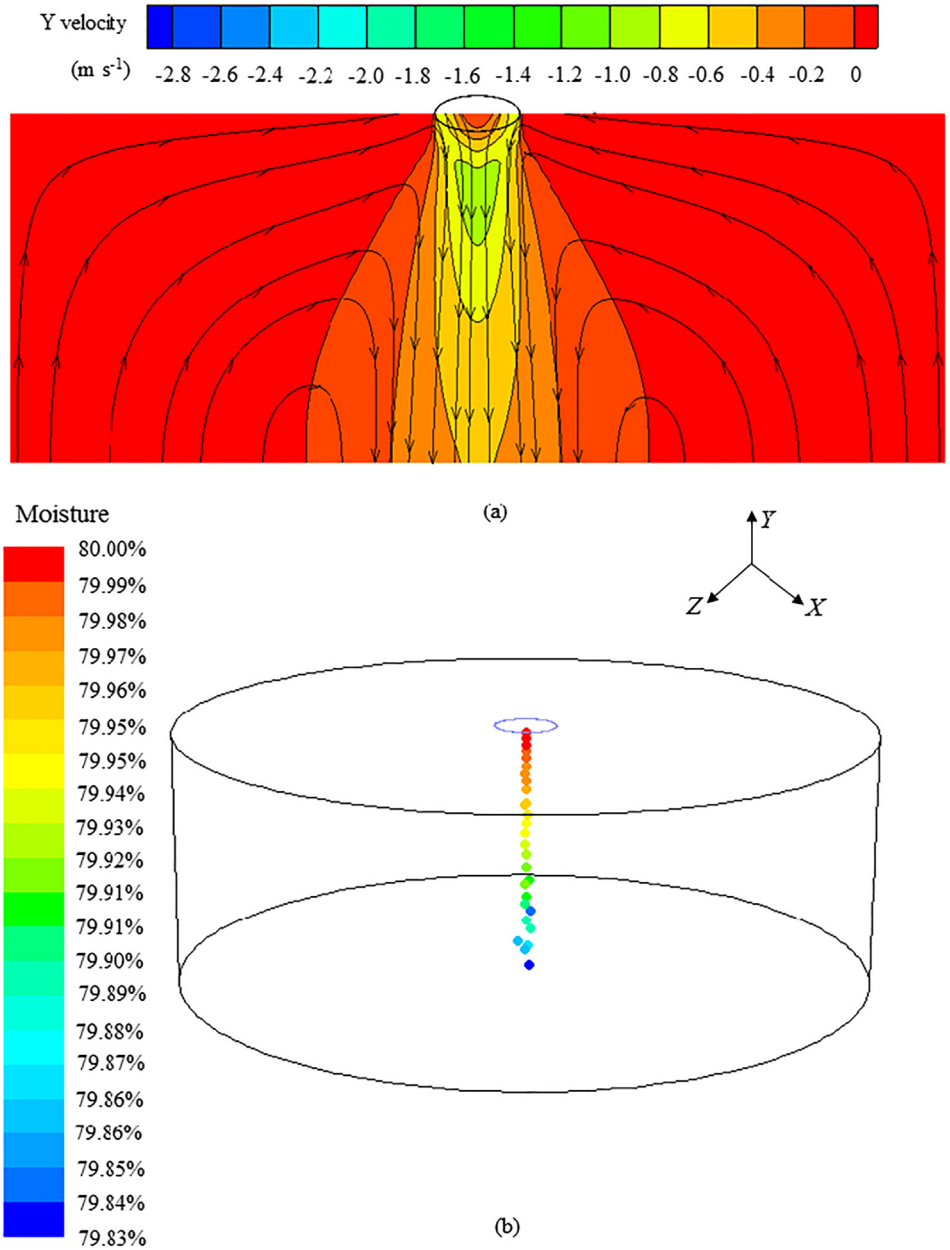

Fig. 5. Multi-phase flow field in the dispersion chamber: (a) streamline and contours of the air flow, and (b) flying droplets.

continue until a pre-specified number of droplet samples have been "collected" at the outlet plane (i.e., the bottom surface of the main dryer).

2.5. Numerical implementation

ICEM CFD is used to mesh the dispersion chamber and the main drying chamber (see Fig. 1). Based on grid independency study, 229,152 mesh cells are used for the dispersion chamber (Xiao et al., 2018), and 162,904 mesh cells are adopted for the main drying chamber (Yang et al., 2015). All models can be solved using ANSYS Fluent. The RNG k-ε turbulence model has been selected to simulate the air flow in both chambers. This turbulence model is known to accurately describe the flow pattern in the spray dryer (Huang et al., 2006). After stability of the air flow, the discrete phase model (DPM) is enabled to characterize the injected droplets in the continuous gas phase. The REA and droplet shrinkage models are coupled via the user-defined functions (UDF).

3. Results and discussion

Numerical simulations of the mono-disperse droplet spray dryer (MDSD) have been carried out to demonstrate the efficacy of the introduced methodology. For the first time, this method allows us to investigate the effect of operational settings on droplet pre-dispersion in the dispersion chamber and hence on the moisture contents of the final particles collected at the dryer outlet. The initial air and droplet conditions used are listed in Tables 1 and 2, and closely represent the real experimental scenarios. The conditions of the base case correspond to 195 μm droplets spray dried at an inlet air temperature of 111 °C. It will serve as an implementation example of the method as well as a comparison base for other cases under different drying temperatures.

3.1. Charactering flying droplets in the dispersion chamber

Before the injection of atomized droplets, the dispersion air flow needs to attain a steady condition. A stable flow field is shown in Fig. 5(a). The injected mono-dispersed droplets fly in this air flow field. Due to air-droplet interaction, dispersion of droplets can be observed (see Fig. 5(b)).

In this study, a total of ~5000 droplets were collected at the bottom surface of the dispersion chamber. Fig. 6 shows 2D distributions of all collected droplets at the bottom surface, i.e., the (x, z) plane. As can be observed, the properties such as $\| \vec{v}_p \|$, T_p, W, and d_p for each droplet have been represented by the colour bars for easy identification. Droplets are mainly located at the plane center owing to the mild turbulent air flow pattern. Larger size droplets with higher moisture content and velocity reach the exit faster. An increase in residence time is always prompted by a decrease in velocity, and thus lower moisture content and higher temperature of droplets. Meanwhile, the temperature of larger size droplets is lower as a result of shorter contact with the air.

Furthermore, in order to obtain a quantitative understanding of droplets dispersion state, the droplet occupied area has been divided into three or four circular slices with each slice having four

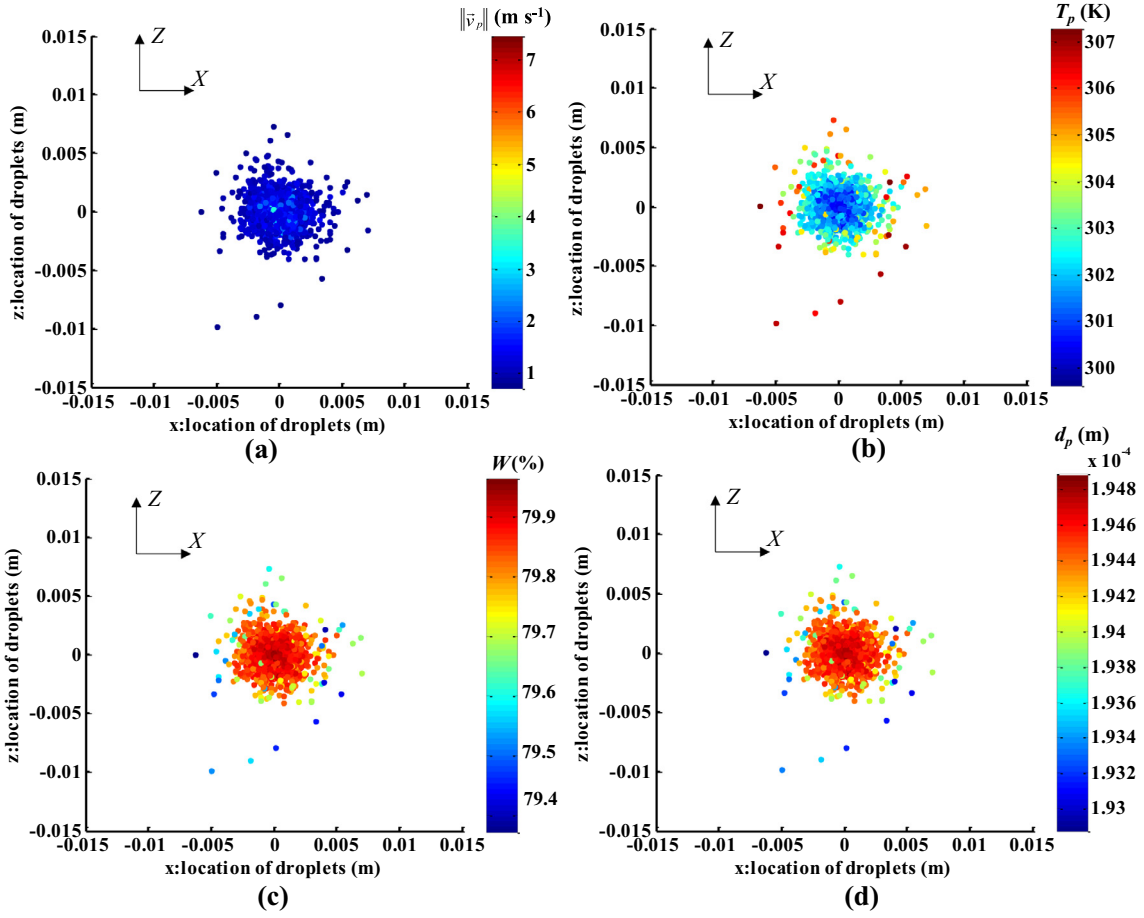

Fig. 6. 2D plots of droplet distribution in the (x, z) outlet plane in which the colorbar represents: (a) velocity magnitude, (b) droplet temperature, (c) moisture content, and (d) droplet size.

zones (schemes 1–4). A 2D statistical analysis of the dispersion of droplets' velocity magnitude, temperature, moisture content and size at each injection for Scheme 4 is shown in Fig. 7. A decreasing trend can be observed for $\| \vec{v}_p \|$, W, d_p and an increasing trend for T_p from the inner layer to the outer layer (k = 1–4). The data also suggest that smaller size droplets move towards the edge of the chamber exit with lower velocity. Temperatures of droplets at the exit edge are higher resulting to their lower moisture contents. These observations are also consistent with the 2D plots given in Fig. 6. Additional information regarding the concentration of droplets at the circular exit is provided in Fig. 8. The data demonstrate that the number distribution of droplets in each layer is uniform for Scheme 4 (Fig. 8(a)). The number percentage distribution is quite similar to the mass flow rate distribution (Fig. 8(b)), because droplet evaporation is insignificant in the dispersion chamber, i.e., less than 0.15% moisture content decrease (see Fig. 7(c)). While it is quite different from the mass flux distribution (Fig. 8(c)), the mass flux in the 4th layer is almost 0 due to the large areas of zones in the 4th layer.

3.2. Creating injections

The droplets exiting dispersion chamber are quite wet. Further drying is performed in the second column (i.e. the main drying chamber) to achieve efficient drying. This study provides a realistic injection scenario of droplets at the inlet of the main drying chamber (i.e., the exit of the dispersion chamber) by resorting to a strategic coupling approach. The MDSD consisting of two chambers with big size difference, for the first time, can be simulated as a holistic unit.

For the purpose of coupling the two chambers, four schemes have been provided (Fig. 4). A droplet injection is created for each

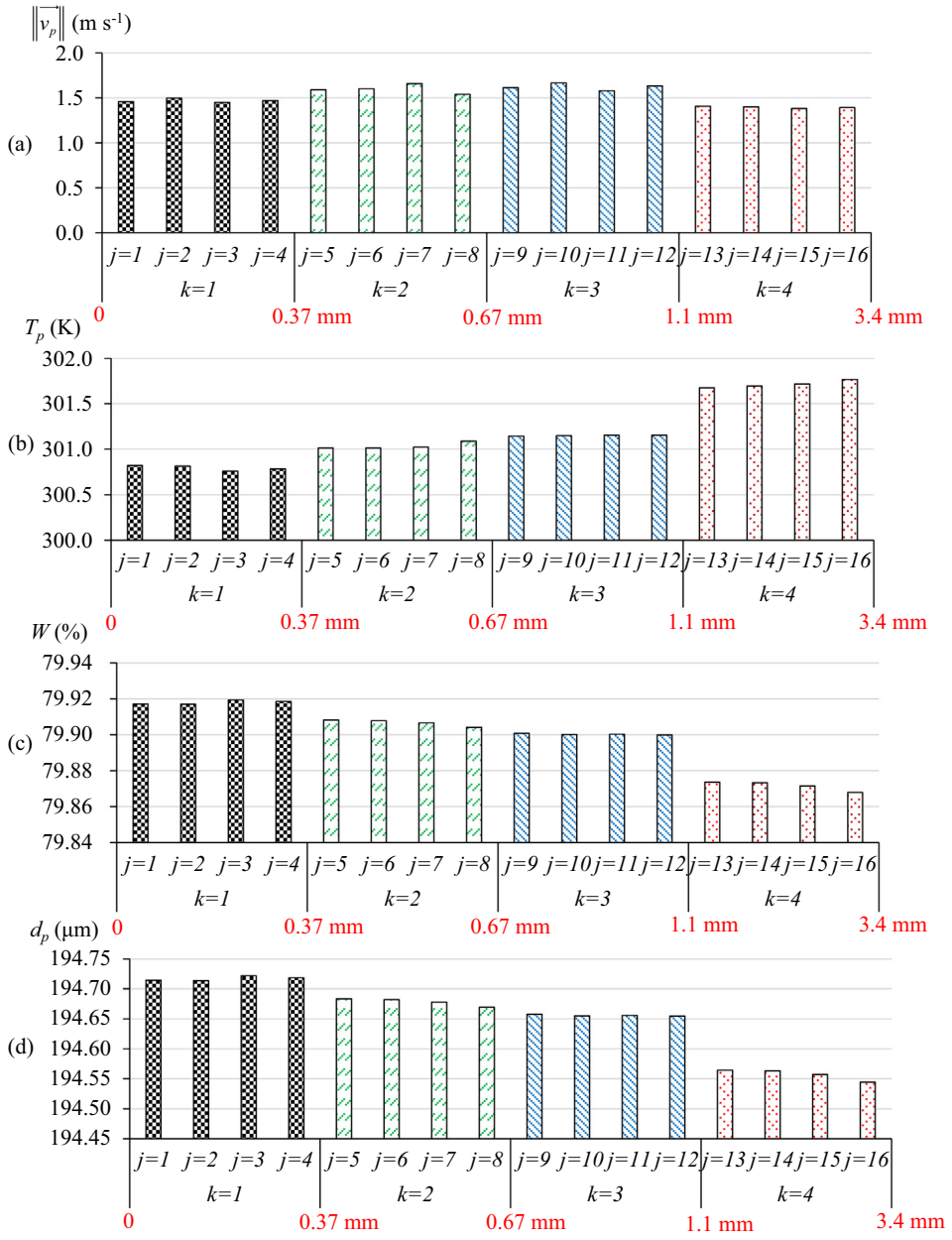

Fig. 7. Droplet distribution at the dispersion chamber outlet divided based on Scheme 4: (a) velocity magnitude, (b) droplet temperature, (c) moisture content, and (d) droplet size.

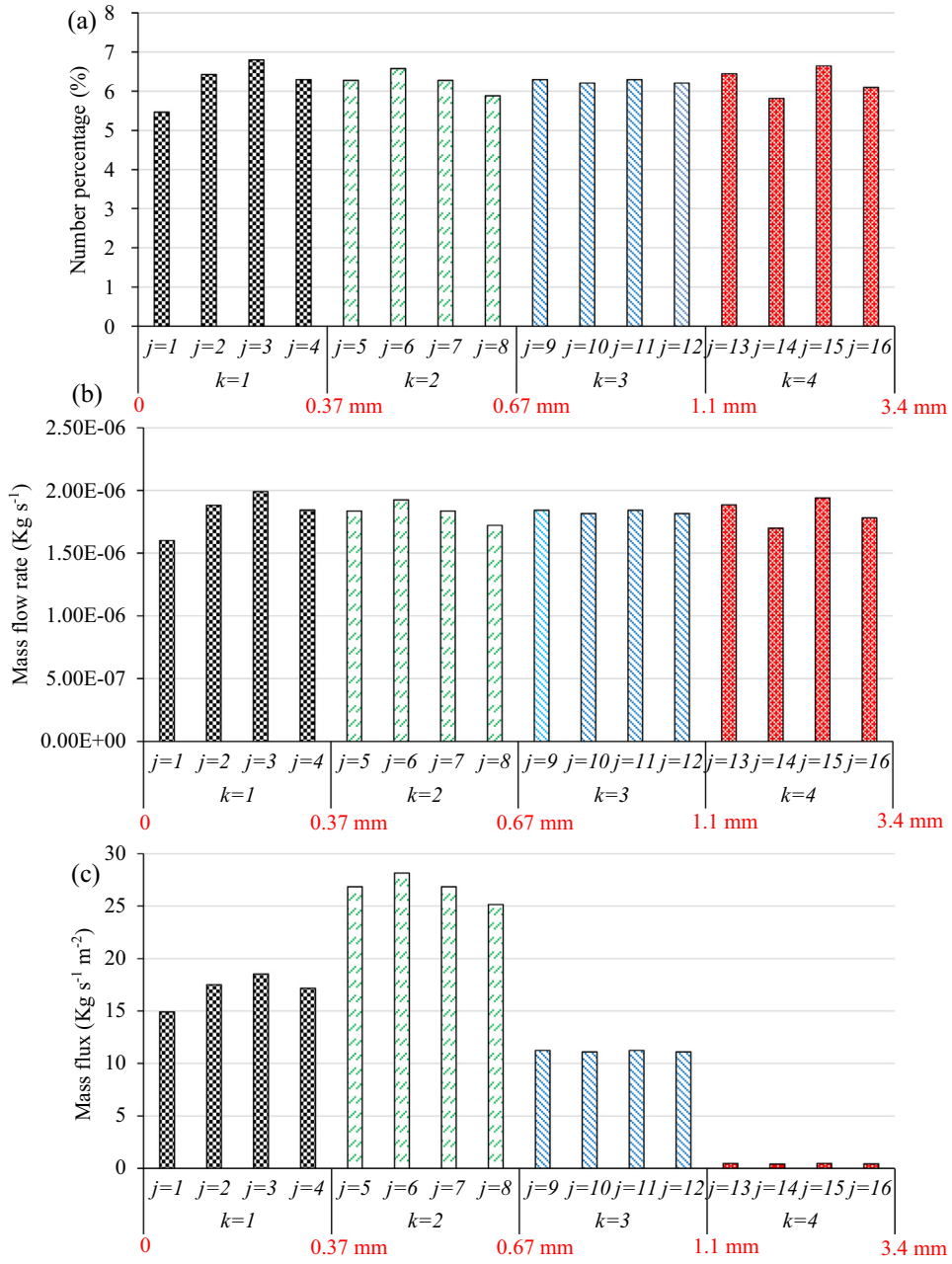

Fig. 8. Droplet distribution at the dispersion chamber outlet divided based on Scheme 4: (a) number percentage, (b) mass flow rate, and (c) mass flux.

Table 3
Parameter settings for 12 injections in Scheme 1 (195 μm droplets of 20 wt% skim milk spray dried at an inlet air temperature of 111 °C).

Zone index	Location (mm)			Velocity (m s^{-1})			Temperature (K)	Diameter (μm)	Mass flow Rate (kg s^{-1})	Moisture content (%)
j	$\bar{x}$	$\bar{y}$	$\bar{z}$	$\bar{u}$	$\bar{v}$	$\bar{w}$	$\bar{T}$	$\bar{d}$	$\dot{M}$	W
1	0.340	0	0.358	0.0148	−1.573	0.0154	300.9872	194.69	5.481e−6	79.91
2	−0.335	0	0.345	−0.0143	−1.583	0.0148	301.0075	194.68	5.501e−6	79.91
3	−0.346	0	−0.332	−0.0147	−1.558	−0.0140	300.9715	194.69	5.635e−6	79.91
4	0.343	0	−0.341	0.0144	−1.541	−0.0146	301.0035	194.68	5.367e−6	79.91
5	0.973	0	0.970	0.0309	−1.450	0.0308	301.5463	194.59	1.508e−6	79.88
6	−0.999	0	0.970	−0.0323	−1.443	0.0310	301.5595	194.59	1.451e−6	79.88
7	−1.029	0	−0.957	−0.0334	−1.447	−0.0319	301.5785	194.58	1.426e−6	79.88
8	0.975	0	−0.984	0.0313	−1.436	−0.0320	301.5481	194.59	1.560e−6	79.88
9	1.813	0	1.718	0.0434	−1.162	0.0403	302.3840	194.45	3.049e−7	79.84
10	−1.845	0	1.625	−0.0431	−1.173	0.0382	302.3900	194.44	3.303e−7	79.84
11	−1.816	0	−1.620	−0.0431	−1.170	−0.0353	302.4456	194.42	3.620e−7	79.83
12	1.680	0	−1.879	0.0427	−1.179	−0.0433	302.4557	194.43	3.239e−7	79.83

Table 4
Parameter settings for 16 injections in Scheme 2 (195 μm droplets of 20 wt% skim milk spray dried at an inlet air temperature of 111 °C).

Zone index	Location (mm)			Velocity (m s^{-1})			Temperature (K)	Diameter (μm)	Mass flow Rate (kg s^{-1})	Moisture content (%)
j	$\bar{x}$	$\bar{y}$	$\bar{z}$	$\bar{u}$	$\bar{v}$	$\bar{w}$	$\bar{T}$	$\bar{d}$	$\dot{M}$	W
1	0.210	0	0.208	0.0096	−1.523	0.0091	300.8857	194.70	2.978e−6	79.91
2	−0.201	0	0.205	−0.0083	−1.539	0.0091	300.9071	194.70	3.156e−6	79.91
3	−0.203	0	−0.196	−0.0094	−1.538	−0.0088	300.8466	194.71	3.245e−6	79.91
4	0.195	0	−0.201	0.0089	−1.482	−0.0085	301.9072	194.70	3.003e−6	79.91
5	0.494	0	0.536	0.0208	−1.632	0.0228	301.1080	194.66	2.504e−6	79.90
6	−0.514	0	0.533	−0.0223	−1.643	0.0225	301.1426	194.66	2.345e−6	79.90
7	−0.540	0	−0.518	−0.0219	−1.585	−0.0211	301.1413	194.66	2.389e−6	79.90
8	0.531	0	−0.518	0.0213	−1.617	−0.0224	301.1257	194.66	2.364e−6	79.90
9	0.973	0	0.970	0.0309	−1.450	0.0308	301.5463	194.59	1.509e−6	79.88
10	−0.999	0	0.970	−0.0323	−1.443	0.0310	301.5595	194.59	1.451e−6	79.88
11	−1.029	0	−0.957	−0.0334	−1.447	−0.0319	301.5785	194.58	1.426e−6	79.88
12	0.975	0	−0.984	0.0313	−1.436	−0.0320	301.5481	194.59	1.560e−6	79.88
13	1.813	0	1.718	0.0434	−1.162	0.0403	302.3840	194.45	3.049e−7	79.84
14	−1.845	0	1.625	−0.0431	−1.173	0.0382	302.3900	194.44	3.303e−7	79.84
15	−1.816	0	−1.620	−0.0431	−1.170	−0.0353	302.4456	194.42	3.620e−7	79.83
16	1.680	0	−1.879	0.0427	−1.179	−0.0433	302.4557	194.43	3.239e−7	79.83

Table 5
Parameter settings for 16 injections in Scheme 3 (195 μm droplets of 20 wt% skim milk spray dried at an inlet air temperature of 111 °C).

Zone index	Location (mm)			Velocity (m s^{-1})			Temperature (K)	Diameter (μm)	Mass flow Rate (kg s^{-1})	Moisture content (%)
j	$\bar{x}$	$\bar{y}$	$\bar{z}$	$\bar{u}$	$\bar{v}$	$\bar{w}$	$\bar{T}$	$\bar{d}$	$\dot{M}$	W
1	0.137	0	0.134	0.0063	−1.459	0.0063	300.8188	194.71	1.601e−6	79.92
2	−0.137	0	0.140	−0.0054	−1.498	0.0066	300.8166	194.71	1.881e−6	79.92
3	−0.133	0	−0.130	−0.0058	−1.451	−0.0055	300.7587	194.72	1.990e−6	79.92
4	0.121	0	−0.143	0.0062	−1.469	−0.0064	300.7835	194.72	1.843e−6	79.92
5	0.325	0	0.327	0.0152	−1.627	0.0142	300.9733	194.69	2.021e−6	79.91
6	−0.324	0	0.331	−0.0141	−1.589	0.0142	301.0693	194.67	1.804e−6	79.91
7	−0.341	0	−0.332	−0.0155	−1.651	−0.0332	301.0197	194.68	1.791e−6	79.91
8	0.331	0	−0.331	0.0136	−1.523	−0.0139	301.0798	194.67	1.702e−6	79.91
9	0.533	0	0.579	0.0217	−1.616	0.0243	301.1432	194.66	1.841e−6	79.90
10	−0.549	0	0.570	−0.0237	−1.666	0.0240	301.1491	194.66	1.816e−6	79.90
11	−0.576	0	−0.549	−0.0233	−1.581	−0.0224	301.1529	194.66	1.841e−6	79.90
12	0.578	0	−0.549	0.0234	−1.631	−0.0235	301.1544	194.65	1.816e−6	79.90
13	1.105	0	1.101	0.0327	−1.401	0.0325	301.6856	194.56	1.833e−6	79.87
14	−1.156	0	1.092	−0.0343	−1.393	0.0323	301.7135	194.56	1.782e−6	79.87
15	−1.186	0	−1.088	−0.0354	−1.394	−0.0326	301.7503	194.55	1.801e−6	79.87
16	1.096	0	−1.136	0.0333	−1.393	−0.0340	301.7026	194.56	1.890e−6	79.87

Table 6
Parameter settings for 16 injections in Scheme 4 (195 μm droplets of 20 wt% skim milk spray dried at an inlet air temperature of 111 °C).

Zone index	Location (mm)			Velocity (m s^{-1})			Temperature (K)	Diameter (μm)	Mass flow Rate (kg s^{-1})	Moisture content
j	$\bar{x}$	$\bar{y}$	$\bar{z}$	$\bar{u}$	$\bar{v}$	$\bar{w}$	$\bar{T}$	$\bar{D}$	$\dot{M}$	W
1	0.137	0	0.134	0.0063	−1.459	0.0063	300.8188	194.71	1.601e−6	0.7992
2	−0.137	0	0.140	−0.0054	−1.498	0.0066	300.8166	194.71	1.881e−6	0.7992
3	−0.133	0	−0.130	−0.0058	−1.451	−0.0055	300.7587	194.72	1.990e−6	0.7992
4	0.121	0	−0.143	0.0062	−1.469	−0.0064	300.7835	194.72	1.843e−6	0.7992
5	0.464	0	0.0174	0.0197	−1.627	0.00047	301.0134	194.68	1.836e−6	0.7991
6	0.0198	0	0.464	0.00129	−1.603	0.0205	301.0136	194.68	1.925e−6	0.7991
7	−0.465	0	−0.332	−0.0208	−1.661	−0.00105	301.0226	194.68	1.836e−6	0.7991
8	−0.0062	0	−0.475	0.00018	−1.540	−0.0201	301.0869	194.67	1.721e−6	0.7991
9	0.533	0	0.579	0.0217	−1.616	0.0243	301.1432	194.66	1.841e−6	0.7990
10	−0.549	0	0.570	−0.0237	−1.666	0.0240	301.1491	194.66	1.816e−6	0.7990
11	−0.576	0	−0.549	−0.0233	−1.581	−0.0224	301.1529	194.66	1.841e−6	0.7990
12	0.578	0	−0.549	0.0234	−1.631	−0.0235	301.1544	194.65	1.816e−6	0.7990
13	1.538	0	0.0224	0.0463	−1.406	−0.00039	301.6747	194.56	1.884e−6	0.7987
14	0.00016	0	1.571	0.00062	−1.400	0.0468	301.6942	194.56	1.699e−6	0.7987
15	−1.607	0	−0.0043	−0.0472	−1.382	−0.00028	301.7164	194.56	1.941e−6	0.7987
16	0.0069	0	−1.598	0.00079	−1.393	−0.0472	301.7668	194.54	1.781e−6	0.7987

zone. Settings of droplet injections can be obtained by Eqs. (12)–(17). Those settings for each scheme are listed in Tables 3–6. The mass flow rates of droplets injected at the central layer using schemes 1 and 2 are about ten times more than the droplets injected at the outer layer (see Tables 3 and 4). Whereas, those for schemes 3 and 4 are uniformly distributed across the division layers of the exit plane. The mass flow rate variations for different design schemes may impact the final moisture of the particles.

Data in Tables 3–6 also show that the closer the droplet position to the edge of the plane, the higher is its temperature. Meanwhile, the droplet size becomes smaller towards the edge.

3.3. Predicting particle product property

Temperature profile in the drying chamber directly affects particle product quality. High temperature can cause skim milk degeneration while low temperature can result in the insufficient drying. Experimental results of temperature distribution in an MDSD have been reported by Rogers (2011). The overall heat loss coefficients for the wall of the dryer have been identified to match the temperature distribution along the axis of the main drying chamber with the experimental data (see Table 2). Fig. 9 shows that the model can satisfactorily predict dryer temperature under different hot air inlet temperatures.

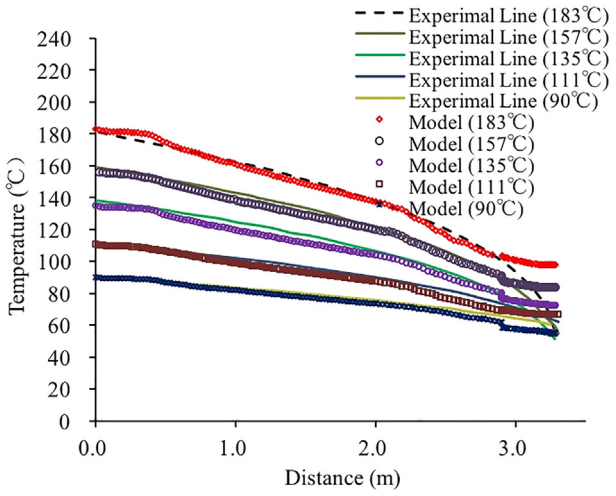

Fig. 9. The temperature profiles in the main drying chamber under different inlet hot air temperatures: simulation results vs. experimental data.

The moisture content dynamics in the main dryer under different coupling schemes are presented in Fig. 10. The present predictions have also been compared with the simulation result of the case neglecting the dispersion chamber. As shown in Fig. 10(a), without the dispersion chamber, a single stream of droplets is directly injected into the main drying chamber, which spreads out while moving down the tower. Multiple streams of droplets are injected into the main drying chamber based on the coupling schemes 1–4 (see Fig. 10(b)–(e)). It is observed that the droplet cloud in Fig. 10(a) is thinner than others close to the dryer ceiling.

The final moisture contents of particles are shown in Fig. 11. Neglecting the dispersion chamber results in ~2% higher moisture content. It should be pointed out that 2% difference in the moisture content for the milk powder product is a "big" difference. The moisture content of milk powder on sale is conventionally controlled at a level very close to 4%. Otherwise, it will lead to product quality problems. Consequently, droplet dispersion should not be neglected. Droplet dispersion promotes mass transfer and heat transfer between droplets and the drying air, hence achieving a lower moisture content without the need to increase the inlet hot air temperature. Noticeable variations of the final moisture content for all the coupling schemes can be identified (Fig. 11),

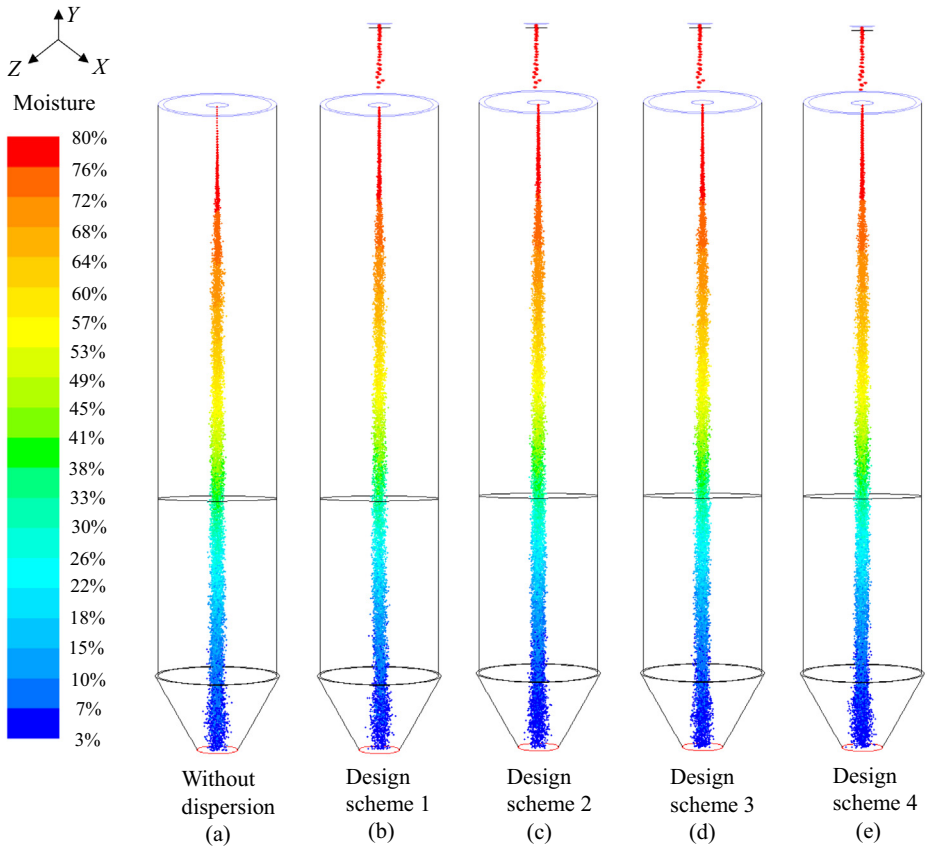

Fig. 10. The droplets' spatial and moiture content distributions in the dispersion and drying chambers: (a) without the dispersion chamber, 1 injection location for the drying chamber, (b) coupling scheme 1, 12 injections for the drying chamber, (c) coupling scheme 2, 16 injections for the drying chamber, (d) coupling scheme 3, 16 injections for the drying chamber, and (e) coupling scheme 4, 16 injections for the drying chamber.

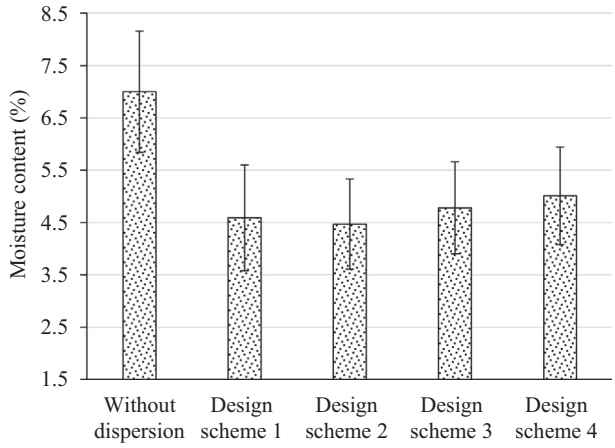

Fig. 11. Comparison of the moisture contents of particles at the dryer outlet. 195 μm droplets were spray dried at an inlet air temperature of 111 °C.

especially between the uniform mass flow rate based division scenario (schemes 3 and 4) and the uniform layer thickness based division scenario (schemes 1 and 2). Thus, selecting appropriate coupling scheme that could better capture droplet dispersion states becomes important. Scheme 4 has been chosen for subsequent computations. This scheme better captures droplet flux across the coupling interface and adopts rotated locations of droplet injections between division layers.

The final moisture contents at different inlet air temperatures and droplet size conditions have been compared with experimental measurements. As shown in Fig. 12, the trend of predictions is consistent with the experimental data, i.e., increasing inlet air temperature leads to the decrease of particle moisture content. At low air inlet temperatures, there is a smaller temperature difference between the atomized feed and the drying air, resulting in a lesser driving force for water evaporation and thus producing powders with higher moisture content (George et al., 2015). The final moisture content is heavily dependent on the initial droplet size while the measured droplet size has deviations (see the droplet size data listed in Fig. 12). Prediction results under three sets of initial droplet diameters are plotted, i.e., the maximum diameter (green triangles), the mean diameter (red diamonds), and the minimum diameter (blue circles). It is observed that predicted range covers the experimental data well at the temperature lower than 140 °C. A consistent underestimation can be observed for inlet air temperatures above 140 °C regardless of the initial droplet size. It is because dry particles encounter moisture reabsorption during the moisture measurement process after drying (Yang et al., 2015), which leads to lower simulated moisture contents than experimental values. A moisture reabsorption model can be included in the future to take this issue into account.

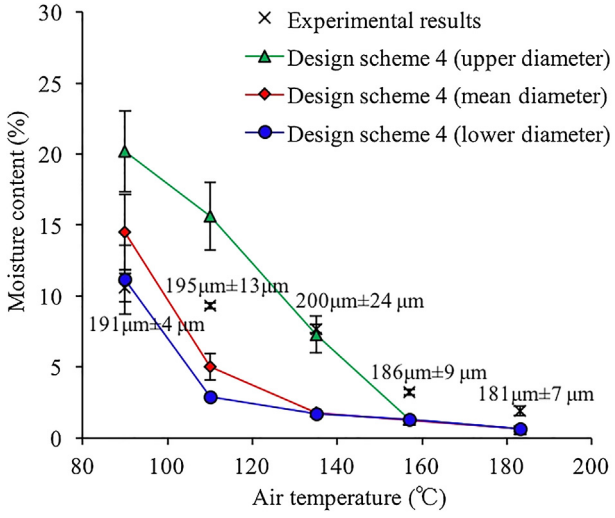

Fig. 12. Particle final moisture content for different sized droplets spray dried under different hot air inlet temperatures: model predictions vs. experimental measurements. Initial droplet diameters with deviations used in experiments are listed. Prediction results are under three sets of initial droplet diameters, i.e., the maximum diameter (green triangles), the mean diameter (red diamonds), and the minimum diameter (blue circles). (For interpretation of the references to color in this figure legend, the reader is referred to the web version of this article.)

4. Conclusion

In this study, a systematic coupling approach is introduced to deal with a type of challenging DPM simulations where discrete-phase droplets need to fly across consecutive chambers with distinctively different sizes. The difficulty of solving DPM models in multiple chambers as a single unit arises from chambers' geometric size differences. The introduced method has been successfully utilized to investigate the spray drying process in the monodisperse droplet spray dryer (MDSD), which consists of a small dispersion chamber and a big drying chamber. Droplet samples are collected at the exit of the dispersion chamber, and then used as the input conditions in the second stage for the main dryer. Four coupling schemes have been designed to create droplet injections into the main dryer based on rigorous mass, momentum and energy conservation laws. For the first time, the MDSD is simulated as a holistic unit, where droplet drying can be characterized from the nozzle outlet to the exit of the dryer. Model predictions of particles' final moisture contents have been validated using experimental measurements. This model allows future explorations of optimized droplet dispersion operations towards energy-efficient and quality-ensured spray drying in the MDSD. One of the most recent efforts is to introduce swirling flow into the dryer for drying efficiency improvement (Yang et al., 2018). The general coupling method is generic and should be applicable to some industrial practices that need to study flying droplets across multiple chambers with significantly different sizes.

Acknowledgment

We are grateful for the financial support from the Natural Science Foundation of Jiangsu Province (BK20170062), the National Key Research and Development Program of China (International S&T Cooperation Program, ISTCP, 2016YFE0101200), the National Natural Science Foundation of China (21406148), the "Jiangsu Innovation and Entrepreneurship (Shuang Chuang) Program", the "Jiangsu Specially-Appointed Professors Program", and the "Priority Academic Program Development (PAPD) of Jiangsu Higher Education Institutions".

References

Baltas, L., Gauvin, W.H., 1969. Transport characteristics of a cocurrent spray dryer. AIChE J. 15 (5), 772–779.
Baldwin, A.J., Truong, G.N.T., 2007. Development of insolubility in dehydration of dairy milk powders. Food Bioprod. Process. 85, 202–208.
Chen, X.D., 2008. The basics of a reaction engineering approach to modeling air-drying of small droplets or thin-layer materials. Dry. Technol. 26, 627–639.
Chen, X.D., Lin, S.X.Q., 2005. Air drying of milk droplet under constant and time-dependent conditions. AIChE J. 51, 1790–1799.
Fletcher, D.F., Langrish, T.A.G., 2009. Scale-adaptive simulation (SAS) modelling of a pilot-scale spray dryer. Chem. Eng. Res. Des. 87, 1371–1378.
Foerster, M., Gengenbach, T., Woo, M.W., Selomulya, C., 2016. The impact of atomization on the surface composition of spray-dried milk droplets. Colloids Surf. B Biointerfaces 140, 460–471.

George, O.A., Chen, X.D., Xiao, J., Woo, M., Che, L., 2015. An effective rate approach to modeling single-stage spray drying. AIChE J. 61, 4140–4151.
Haider, A., Levenspiel, O., 1989. Drag coefficient and terminal velocity of spherical and nonspherical particles. Powder Technol. 58, 63–70.
Huang, L., Kumar, K., Mujumdar, A.S., 2003. Use of computational fluid dynamics to evaluate alternative spray dryer chamber configurations. Dry. Technol. 21, 385–412.
Huang, L.X., Kumar, K., Mujumdar, A.S., 2006. A comparative study of a spray dryer with rotary disc atomizer and pressure nozzle using computational fluid dynamic simulations. Chem. Eng. Process. Process. Intensif. 45, 461–470.
Jin, Y., Chen, X.D., 2009a. Numerical study of the drying process of different sized particles in an industrial-scale spray dryer. Dry. Technol. 27, 371–381.
Jin, Y., Chen, X.D., 2009b. A three-dimensional numerical study of the gas/particle interactions in an industrial-scale spray dryer for milk powder production. Dry. Technol. 27, 1018–1027.
Kavoshi, L., Rahimi, A., Hatamipour, M.S., 2015. CFD modeling and experimental study of carbon dioxide removal in a lab-scale spray dryer. Chem. Eng. Res. Des. 98, 157–167.
Lin, S.X.Q., Chen, X.D., 2004. Changes in milk droplet diameter during drying under constant drying conditions investigated using the glass-filament method. Food Bioprod. Process. 82, 213–218.
Lin, S.X.Q., Chen, X.D., Pearce, D.L., 2005. Desorption isotherm of milk powders at elevated temperatures and over a wide range of relative humidity. J. Food Eng. 68, 257–264.
Liu, W., Wu, W.D., Selomulya, C., Chen, X.D., 2011. Uniform chitosan microparticles prepared by a novel spray-drying technique. Int. J. Chem. Eng. 2011, 1–7.
Mezhericher, M., Levy, A., Borde, I., 2007. Theoretical drying model of single droplets containing insoluble or dissolved solids. Dry. Technol. 25, 1025–1032.
Mezhericher, M., Levy, A., Borde, I., 2008. Droplet-droplet interactions in spray drying by using 2D computational fluid dynamics. Dry. Technol. 26, 265–282.
Mezhericher, M., Levy, A., Borde, I., 2014. Multi-scale multiphase modeling of transport phenomena in spray-drying processes. Dry. Technol. 33, 2–23.
Patel, K., Chen, X.D., Jeantet, R., Schuck, P., 2010. One-dimensional simulation of co-current, dairy spray drying systems – pros and cons. Dairy Sci. Technol. 90, 181–210.
Patel, K.C., Chen, X.D., 2008. Drying of aqueous lactose solutions in a single stream dryer. Food Bioprod. Process. 86, 185–197.
Patel, K.C., Chen, X.D., Lin, S.X.Q., Adhikari, B., 2009. A composite reaction engineering approach to drying of aqueous droplets containing sucrose, maltodextrin (DE6) and their mixtures. AIChE J. 55, 217–231.
Pawar, S., Padding, J., Deen, N., Jongsma, A., Innings, F., Kuipers, J.A.M., 2015. Numerical and experimental investigation of induced flow and droplet–droplet interactions in a liquid spray. Chem. Eng. Sci. 138, 17–30.
Putranto, A., Chen, X.D., 2016. Drying of a system of multiple solvents: modeling by the reaction engineering approach. AIChE J. 62, 2144–2153.
Ré, M.-I., 2006. Formulating drug delivery systems by spray drying. Dry. Technol. 24, 433–446.
Ranz, W.E., Marshall, W.R., 1952a. Evaporation from drops – Part 1. Chem. Eng. Prog. 48, 141–146.
Ranz, W.E., Marshall, W.R., 1952b. Evaporation from drops – Part 2. Chem. Eng. Prog. 48, 173–180.
Rogers, S., Fang, Y., Qi Lin, S.X., Selomulya, C., Dong Chen, X., 2012. A monodisperse spray dryer for milk powder: Modelling the formation of insoluble material. Chem. Eng. Sci. 71, 75–84.
Rogers, S., 2011. Developing and utilizing a mini food powder producion facility to produce industrially relevant particles for functionality testing Ph.D thesis. Monash University, Australia.
Sagadin, G., Hriberšek, M., 2017. A multistage spray drying model for zeolite 4A – water suspensions in a counter-current spray dryer. Int. J. Heat Mass Transf. 108, 1220–1228.
Schmitz-Schug, I., Kulozik, U., Foerst, P., 2016. Modeling spray drying of dairy products – Impact of drying kinetics, reaction kinetics and spray drying conditions on lysine loss. Chem. Eng. Sci. 141, 315–329.
Shakiba, S., Mansouri, S., Selomulya, C., Woo, M.W., 2016. In-situ crystallization of particles in a counter-current spray dryer. Adv. Powder Technol. 27 (6), 2299–2307.
Song, C., Pei, B., Jiang, M., Wang, B., Xu, D., Chen, Y., 2016. Numerical analysis of forces exterted on particles in cyclone separators. Powder Technol. 294, 437–448.
Vicente, J., Pinto, J., Menezes, J., Gaspar, F., 2013. Fundamental analysis of particle formation in spray drying. Powder Technol. 247, 1–7.
Vojir, D.J., Michaelides, E.E., 1994. Effect of the history term on the motion of rigid spheres in a viscous fluid. Int. J. Multiph. Flow 20 (3), 547–556.
Woo, M.W., Wan, W.R., Mujumdar, A.S., Wu, Z.H., Meor, M.T., Tasirin, S.M., 2008. CFD evaluation of droplet drying models in a spray dryer fitted with a rotary atomizer. Dry. Technol. 26 (10), 1180–1198.
Woo, M.W., Rogers, S., Lin, S.X.Q., Selomulya, C., Chen, X.D., 2011. Numerical probing of a low velocity concurrent pilot scale spray drying tower for mono-disperse particle production – Unusual characteristics and possible improvements. Chem. Eng. Process. Process Intensif. 50, 417–427.
Woo, M.W., Rogers, S., Selomulya, C., Chen, X.D., 2012. Particle drying and crystallization characteristics in a low velocity concurrent pilot scale spray drying tower. Powder Technol. 223, 39–45.
Xiao, J., Chen, X.D., 2014. Multiscale modeling for surface composition of spray-dried two-component powders. AIChE J. 60, 2416–2427.
Xiao, J., Li, Y., George, O.A., Li, Z.H., Yang, S.J., Woo, M.W., Wu, W.D., Chen, X.D., 2018. Numerical investigation of droplet pre-dispersion in a monodisperse droplet spray dryer. Particuology 38, 44–60.
Yang, S.J., Wei, Y.C., Woo, M.W., Wu, W.D., Chen, X.D., Xiao, J., 2018. Numerical simulation of mono-disperse droplet spray dryer under influence of swirling flow. J. Chem. Ind. Eng. (China) (CIESC J.) 69 (9), 3814–3824.
Yang, X.F., Xiao, J., Woo, M.-W., Chen, X.D., 2015. Three-dimensional numerical investigation of a mono-disperse droplet spray dryer: validation aspects and multi-physics exploration. Dry. Technol. 33, 742–756.
You, X., Zhou, Z.H., Liao, Z.K., Che, L.M., Chen, X.D., Wu, W.D., Woo, M.W., Selomulya, C., 2014. Dairy milk particles made with a mono-disperse droplet spray dryer (MDDSD) investigated for the effect of fat. Dry. Technol. 32, 528–542.
Zastawny, M., Mallouppas, G., Zhao, F., van Wachem, B., 2012. Derivation of drag and lift force and torque coefficients for non-spherical particles in flows. Int. J. Multiph. Flow 39, 227–239.